PHYSICAL REVIEW B **104**, 035132 (2021)

Negative magnetization induced by particle-size reduction in $\mathrm{Gd}_{1-x}\mathrm{Ca}_x\mathrm{MnO}_3$ nanoparticle systems

Papri Dasgupta,[1,*] Sanjukta Paul,[3] Nirmal Mondal,[1] S. Kumar,[1,†] Sudhakar Yarlagadda,[2,‡] and Chandan Mazumdar[2,§]
[1] *Physics Department, Jadavpur University, Kolkata 700032, India*
[2] *CMP Division, Saha Institute of Nuclear Physics, Kolkata 700064, India*
[3] *School of Physical Sciences, National Institute of Science Education and Research, Jatni 752050, India*

(Received 13 April 2021; revised 28 June 2021; accepted 1 July 2021; published 16 July 2021)

We report a pervasive phenomenon of gradual emergence of negative magnetization in typical $R_{1-x}D_x\mathrm{MnO}_3$ orthorhombic perovskite manganites in nanoform (with R^{3+} being a trivalent high-magnetic-moment ion from the heavier rare-earth elements Gd, Tb, Dy and D^{2+} refers to divalent alkaline elements Sr, Ca, etc.), while the bulk form manifests no negative magnetization. Extensive magnetization studies have been carried out in $\mathrm{Gd}_{1-x}\mathrm{Ca}_x\mathrm{MnO}_3$ around half doping. We demonstrate experimentally that particle size reduction in nano-form manganites enhances the propensity of the system to exhibit negative magnetization and propose a theoretical explanation for the phenomenon. To test the universality of our findings, we have extended the measurement to $\mathrm{Dy}_{0.6}\mathrm{Ca}_{0.4}\mathrm{MnO}_3$ and obtained similar results.

DOI: 10.1103/PhysRevB.104.035132

I. INTRODUCTION

Over the past few decades, complex oxides such as manganites have attracted intense research interest. They display a fascinating tapestry of charge, spin, and orbital orders when a trivalent rare-earth element is replaced by a divalent alkaline element [1–7]. The rare-earth manganites $R\mathrm{MnO}_3$, for the compounds with rare-earth element $R =$ La–Dy, exhibit an orthorhombic perovskite structure; on the other hand, compounds with $R =$ Ho–Lu form in hexagonal structure [8,9].

A large amount of research has focused on features of pure and doped $R\mathrm{MnO}_3$ when R is a light rare-earth element with a weak magnetic moment and large ionic radius. On the other hand, insufficient attention has been paid to pure and doped perovskite manganites involving heavy rare-earth elements (with large effective moment and small ionic size [10]) such as $R =$ Gd, Tb, and Dy and divalent alkaline dopant elements Sr, Ca, etc. Due to the usage of small-sized elements (Gd, Tb, and Dy), a few important modifications have to be taken into account—the tolerance factor decreases and the buckling and tilting of the ideal cubic structure becomes pronounced. Additionally, interesting cooperative effects manifest due to the large magnetic moment of the ions in the rare-earth network—namely, a reversal of the magnetization results due to the coupling of the two interacting magnetic networks [11,12]. Furthermore, these manganites, $R\mathrm{MnO}_3$ ($R =$ Gd, Tb, and Dy), display multiferroicity with magnetic order being accompanied by electric polarization [13–17].

Although permanent magnetic systems generally show positive magnetization values, there are some systems (having two sublattices) which may exhibit negative magnetization, i.e., the direction of the total magnetization is opposite to that of a weak external magnetic field (H_{ext}) meant to align the net magnetic moment. Negative magnetization can result due to negative-exchange coupling between two ferromagnetically ordered sublattices [11]. However, two individually ferromagnetic sublattices are not always needed for the manifestation of negative magnetization. There exists another interesting set of compounds that also display negative magnetization, wherein a disordered paramagnetic sublattice is coupled with an ordered ferromagnetic subtlattice via negative-exchange interaction. In these compounds having two sublattices A and B, sublattice A orders along the external field below a magnetic ordering temperature T_{C} and influences the sublattice B (which remains paramagnetic at the measuring temperature $T \geqslant T_{\mathrm{C}}$) to align opposite to the field of sublattice A. Below a certain temperature called the compensation temperature (which is sizeably smaller than T_{C}), if the moment of sublattice B becomes larger than that of A, the net magnetization becomes negative [11,12]. A finite magnetic anisotropy should also be present in the system to prevent the rotation of the net magnetic moment, below the compensation temperature, in the direction of applied magnetic field. Some examples of such compounds are orthorhombic perovskite manganites $R_{1-x}D_x\mathrm{MnO}_3$ with R^{3+} being Gd, Tb, and Dy and D^{2+} referring to Sr or Ca [11,12,18–25].

In recent years, research on compounds exhibiting negative magnetization has been gaining momentum as these materials can be utilized in digital data storage systems by exploiting their ability to reversibly switch between two distinct magnetization states (i.e., positive and negative) when the temperature or an externally applied magnetic field or light is varied [11,26]. Bipolar switching of the magnetization can be employed to make magnetoelectronic devices such as volatile memories. Furthermore, the low cost of synthesis of manganites by the sol-gel technique makes them suitable for large-scale industrial application [27].

---

[*] paprisengupta@gmail.com
[†] kumar_dsa@yahoo.com
[‡] y.sudhakar@saha.ac.in
[§] chandan.mazumdar@saha.ac.in

Generally, among the perovskite manganites, negative magnetization can be obtained in a low-bandwidth material having mixed-valent Mn ions (i.e., Mn^{3+} and Mn^{4+}). Low bandwidth can be realized in systems containing the heavier rare-earth elements (Gd–Dy) [12]; mixed valency of Mn ions is obtained by partially substituting trivalent rare-earth ions by divalent alkaline-earth ions. These undoped heavier rare-earth manganites, including $GdMnO_3$ (whose doped version is studied here), have been reported to exhibit antiferromagnetic (AFM) insulating behavior [14,18]. We have chosen Gd-based manganites because of the simplicity resulting from the zero orbital angular momentum in Gd^{3+} ions. With the substitution of divalent ions (e.g., Ca^{2+}), an equivalent number of Mn^{4+} ions are introduced in the Mn sublattice of $Gd_{1-x}Ca_xMnO_3$ to make the system charge neutral. With the Gd ions remaining paramagnetic down to low temperatures, the Mn-Mn interaction leads to different ordered states in $Gd_{1-x}Ca_xMnO_3$ depending on the relative percentage of Mn^{3+} and Mn^{4+} ions. The phase diagram of $Gd_{1-x}Ca_xMnO_3$, obtained from magnetoresistive measurements, reports ferromagnetic insulating phase for $x < 0.5$, which transforms into a charge ordered (CO) state with AFM interactions for $x \geqslant 0.5$ [18,28]. In the low-doped region ($0 < x < 0.5$), the ferromagnetically ordered Mn spins force the Gd spins to align opposite to its direction, i.e., opposite to H_{ext}, due to a weak negative exchange interaction between them [18]; thus, a ferrimagnet results at very low temperatures. With decreasing temperature, as the contribution of the magnetic moment of paramagnetic Gd ions keeps increasing in the direction opposite to the external magnetic field, the net moment decreases and can become negative. At higher doping concentrations ($x > 0.5$), the AFM domains become larger in extent compared to the ferromagnetic domains and percolate the sample; the paramagnetic Gd spins in the AFM domains are free to align along H_{ext}, causing the total magnetization to increase steadily with decreasing temperature [28].

Although the phenomenon of negative magnetization has been studied in manganite compounds in bulk form [11,18,28,29] and in thin-film form [30], the role of particle size in nanoform manganites has not been investigated. In the nanosystems, surface effects in nanoparticles can alter the magnetic behavior. In this paper, we carried out a detailed study of $Gd_{1-x}Ca_xMnO_3$ compounds around half doping (i.e., at $x = 0.4$, 0.5, and 0.6) in their bulk and nanoparticle forms (under the influence of external magnetic fields of various strengths) to understand the effect of particle size on negative magnetization. While the bulk forms of $Gd_{1-x}Ca_xMnO_3$ (at $x = 0.4$ and 0.5) exhibit charge ordering and no signature of negative magnetization, its nanoparticle samples do exhibit negative magnetization at low temperatures although they remain devoid of any charge ordering. However, when temperature is varied, both bulk and nanoforms exhibit a hump in magnetization for $x = 0.4$ and 0.5. In our proposed picture, this is caused by ferromagnetic domains of Mn-spin sublattices aligning at higher temperatures followed by Gd spins in this region aligning antiparallel to the Mn spins at lower temperatures due to a weak AFM Mn-Gd coupling. Furthermore, in the AFM domains of Mn-spin sublattices at any doping, the localized Gd spins in this region (effectively decoupled from the AFM Mn-sublattice) produce a paramagnetic response to the weak external magnetic field. In nanoparticles, owing to the decrease in rigidity of the lattice at the surface, we postulate that the concentration of Gd ions (Ca ions) is higher at the surface (core) because they produce a lower (higher) tolerance factor. Higher than the stoichiometric Gd concentration at $x = 0.4$ and 0.5 yields negative magnetization similar to $Gd_{1-x}Ca_xMnO_3$ at lower doping (i.e., lower than $x = 0.4$ and 0.5, respectively) in the bulk/thin-film form [18,30]. Additionally, the magnetization may also be significantly enhanced due to double exchange in the outer shell of the nanoparticles.

The rest of the paper is organized as follows. In Sec. II, we describe both the preparation methods of bulk and nanoparticle samples of $Gd_{1-x}Ca_xMnO_3$, as well as the measurements performed. Then, in Sec. III, we provide the theoretical framework employed to analyze the observed magnetization and charge ordering. Next, in Sec. IV, we present our data showing the increase in propensity for negative magnetization as the particle size decreases in nanoform samples at various dopings and propose a mechanism for this phenomenon. We close in Sec. V with our concluding observations and discuss possible future directions.

II. EXPERIMENTAL DETAILS

Polycrystalline samples of $Gd_{1-x}Ca_xMnO_3$ ($x = 0.4$, 0.5, 0.6) have been prepared by the well-known sol-gel technique. For the preparation of $Gd_{1-x}Ca_xMnO_3$, Gd_2O_3, $CaCO_3$, and MnO_2 were used as starting materials. An appropriate amount of oxides were separately dissolved in a HNO_3 solution (Oxalic acid is also added in case of MnO_2). These solutions were mixed and an amount of citric acid equivalent to the total number of moles of metal ions was added under moderate heating and stirring conditions. Subsequently, the mixture was slowly evaporated at 80 °C–90 °C in a water bath resulting in the formation of gel which was heated to 250 °C to remove the organic matter and decompose the nitrates of the gel. The black ash thus obtained was ground and further heated to 550 °C for 5 h to kick off the remaining organic matter and then pelletized. The pellets then finally sintered for 24 h at 1250 °C to obtain bulk samples. $Gd_{1-x}Ca_xMnO_3$ nanoparticles of different sizes have been prepared by subsequently sintering the pellets at 700 °C, 800 °C, 900 °C, 1000 °C, and 1100 °C for 3 h. In the rest of this paper, the corresponding nanoparticle samples are identified by mentioning the sintering temperature after the compound, for example, $Gd_{0.5}Ca_{0.5}MnO_3$ annealed at 700 °C is written as $Gd_{1-x}Ca_xMnO_3$-700. The bulk samples are represented in the paper as $Gd_{1-x}Ca_xMnO_3$-bulk. X-ray diffraction (XRD) study was carried out at room temperature with TTRAX-III diffractometer (M/s Rigaku, Japan) using Cu-$K\alpha$ source having wavelength 1.5406 Å. Lattice parameters have been estimated from XRD patterns using FULLPROF software [31]. Magnetization was measured using a VSM-SQUID magnetometer (M/S Quantum Design Inc, USA). Temperature dependence of magnetization in zero-field-cooled (ZFC) and field-cooled (FC) protocols in the warming cycle has been carried out under different magnetic fields (100 Oe < H < 70 000 Oe) in the temperature range 5 K–330 K. Field dependence of

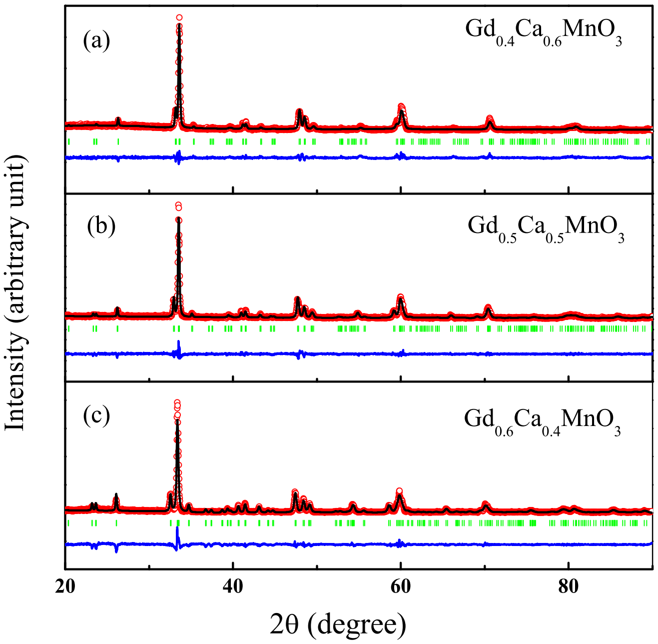

FIG. 1. Room temperature x-ray diffraction pattern of bulk $Gd_{1-x}Ca_xMnO_3$ ($x = 0.4$, 0.5, 0.6) compounds. The experimental data (red points), the calculated (black line) XRD patterns, allowed Bragg position by the space group (green lines), and the difference of experimental data and calculated values (blue lines) for all compounds are displayed.

magnetization (M-H) and magnetic relaxation measurements, etc. have also been carried out.

A room temperature XRD pattern of polycrystalline bulk samples of $Gd_{1-x}Ca_xMnO_3$ ($x = 0.4$, 0.5, 0.6), prepared by the sol-gel technique, is shown in Fig. 1. All the XRD lines confirm the *Pnma* space group, suggesting the materials formed in a single phase within the limit of resolution of our diffraction experiment.

III. THEORETICAL FRAMEWORK

We will analyze magnetization in $Gd_{1-x}Ca_xMnO_3$ (GCMO) structures (bulk or nanomaterials) using ZFC, FC, and isothermal hysteresis curves. We first present the following Hamiltonian, involving a single band for simplicity, without sacrificing any essential physics:

$$H = H_{\mathrm{KE}} + H_{\mathrm{pol}} + H_{\mathrm{M}}. \tag{1}$$

The kinetic energy term H_{KE} is given by

$$H_{\mathrm{KE}} = -te^{-\alpha E_p/\hbar\omega} \sum_{\langle i,j\rangle} \left[\cos\left(\frac{\theta_{i,j}}{2}\right) c^{\dagger}{}_i c_j + \mathrm{H.c.}\right], \tag{2}$$

where t is the fermion hopping amplitude that is attenuated by the electron-phonon coupling $(E_p/\hbar\omega)^{1/2}$ with E_p being the polaron energy, ω the optical phonon frequency, and α a constant of the order unity; c_j is the e_g electron destruction operator; $\theta_{i,j}$ is the angle between $S = 3/2$ spins (originating from localized t_{2g} spins) at Mn sites i and j; and $\cos(\theta_{i,j}/2)$ provides the modulation due to large Hund's coupling between the spin of the hopping e_g electron and the spins of the localized t_{2g} electrons [32,33]. Now, the small size of the Gd^{3+} ion (with the size being smaller than the cavity formed by the MnO_6 octahedra, i.e., with the tolerance factor being small) induces buckling of the $Mn - O - Mn$ bonds, leading to a small hopping t; since the electron-phonon coupling is strong, the kinetic energy is small. Then, in the presence of disorder (such as cation disorder), even when the disorder is weak, this leads to localization (in fact, site localization) of electrons [34].

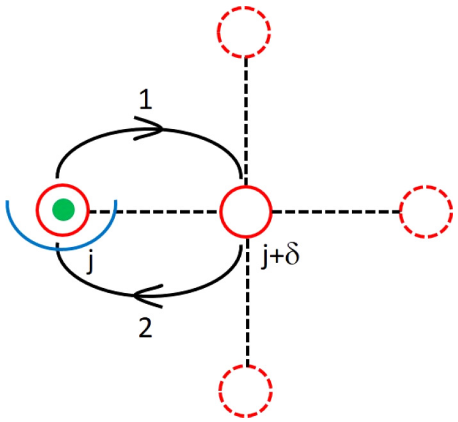

FIG. 2. Hopping process, corresponding to second-order perturbation theory, shown for a two-dimensional Mn lattice. Schematic representation of a fermion, originating at Mn site j, hopping to its NN Mn site $j + \delta$ (the intermediate site) and coming back. Here empty continuous-line circle corresponds to empty site, while continuous-line circle with small dot indicates fermion position. The intermediate site $j + \delta$ has each of its three NN Mn sites (depicted by dashed-line circles) either occupied by a fermion or empty. Semicircle at site j represents full distortion of the lattice ions at that site with corresponding energy $-E_p(+E_p)$ if the fermion is present (absent) at that site.

The second term H_{pol} in Eq. (1) is the polaronic Hamiltonian given by

$$H_{\mathrm{pol}} = -\sum_{j,\delta}\left[\beta E_p + \frac{[t_{j,j+\delta}\cos(\theta_{j,j+\delta}/2)]^2}{2\gamma E_p}\right] n_j(1 - n_{j+\delta}), \tag{3}$$

where the first coefficient βE_p (β being of the order unity) is due to cooperative electron-phonon interaction and portrays nearest-neighbor (NN) electron-electron repulsion due to incompatible distortions of NN oxygen cages surrounding occupied Mn ions. The value of β depends on the nature of compatibility in the orbital order (see Ref. [35]). Next, the second coefficient $[t_{j,j+\delta}\cos(\theta_{j,j+\delta}/2)]^2/(2\gamma E_p)$ results from second-order perturbation theory and involves virtual processes of hopping of a fermion from an Mn site to the NN Mn site and back and is present even when we consider the simpler Holstein model [36]. The factor γ is of the order unity and increases with the increase in occupancy of the neighbors of the Mn site $j + \delta$ (see Fig. 2); this is because of the NN repulsion felt by the fermion when it is virtually present at site $j + \delta$ in the intermediate state of the second-order process [37]. Thus, *the second coefficient in Eq. (3) shows that not only is the NN* Mn *site occupation discouraged,* *the next-NN* Mn *site occupation is also discouraged although to a weaker extent.* Furthermore, although n_j is the total number of electrons in both the e_g orbitals at the Mn site j, it can only take a maximum value of 1 due to strong on-site electron-electron repulsion and strong Hund's coupling. It is important to note that, even though the electrons are localized, the electrons can virtually hop to the neighboring site and produce NN ferromagnetic spin alignment as well as NN, next-NN, and next-to-next-NN charge repulsion through the second coefficient $[t_{j,j+\delta}\cos(\theta_{j,j+\delta}/2)]^2/(2\gamma E_p)$ which is much smaller than the first coefficient βE_p. Thus, the CO energy scale set by the first coefficient βE_p is higher than the ferromagnetic spin-order energy scale set by the second coefficient $[t_{j,j+\delta}\cos(\theta_{j,j+\delta}/2)]^2/(2\gamma E_p)$.

The next term $H_{\rm M}$ in Eq. (1) pertains to the magnetic interactions; in LaMnO$_3$, it refers to the superexchange [38] interactions which generate A-AFM order. In Gd$_{1-x}$Ca$_x$MnO$_3$, it is given by

$$H_{\rm M} = \sum_{\langle i,j\rangle} J_{i,j}\vec{S}_i\cdot\vec{S}_j + J_{\rm Mn-Gd}\sum_{\langle i,\eta\rangle}\vec{S}_i\cdot\vec{\mathcal{S}}_\eta, \tag{4}$$

where $J_{i,j}$ is the Mn − Mn superexchange coupling between the spins on the NNs and $J_{\rm Mn-Gd}$ ($<|J_{i,j}|$) is a weaker AFM coupling between a Gd^{3+} ion at the center of the unit cell (at location η) and its eight NN Mn ions at the corners of the unit cell [20]. In the above expression, the magnitude of the superexchange coefficient $J_{i,j}$ is much smaller than the second coefficient $[t_{j,j+\delta}\cos(\theta_{j,j+\delta}/2)]^2/(2\gamma E_p)$ in Eq. (3). At low temperatures, the AFM coupling $J_{\rm Mn-Gd}$ can produce a metastable state with negative magnetization (actually, a ferrimagnetic state) when at higher temperatures a ferromagnetic state results. The coupling between the rare-earth network and the manganese network is a feature absent in La$_{1-x}$Ca$_x$ MnO$_3$.

IV. RESULTS AND DISCUSSIONS

In this paper, we analyze the magnetic behavior of Gd$_{1-x}$Ca$_x$MnO$_3$ samples at concentrations in the neighborhood of half-doping, i.e., for $x = 0.4$, 0.5, and 0.6. Now, based on the phase diagram for bulk samples (see Ref. [28]), for $x < 0.5$ we have a ferromagnetic insulator, whereas for $0.5 \leqslant x \leqslant 0.8$ we get an AFM insulator at lower temperatures. For $x < 0.5$, based on Ref. [37], the ferromagnetic insulator can be explained as follows. Since cooperative electron-phonon interaction is strong, a NN electron-hole pair has a ferromagnetic interaction $[t_{j,j+\delta}\cos(\theta_{j,j+\delta}/2)]^2/(2\gamma E_p)$ [as shown in Eq. (3)] which is much stronger than other magnetic interactions ($|J_{i,j}|$ and $J_{\rm Mn-Gd}$). Hence, a ferromagnetic cluster (magnetic polaron) is generated in the vicinity of a hole. In fact, the hole (through virtual hopping) will polarize electrons that are NN as well as those that are next-NN and next-to-next-NN to form a magnetic polaron. A collection of interacting magnetic polarons will create a ferromagnetic-insulator region. With respect to the doping region $x \geqslant 0.5$, several theories have been put forth to explain antiferromagnetism [2,4]; we do not propose any new explanation beyond these theories for antiferromagnetism.

We will now provide an understanding of the magnetization displayed in the ZFC, FC, and hysteresis curves for bulk and nanoparticle forms.

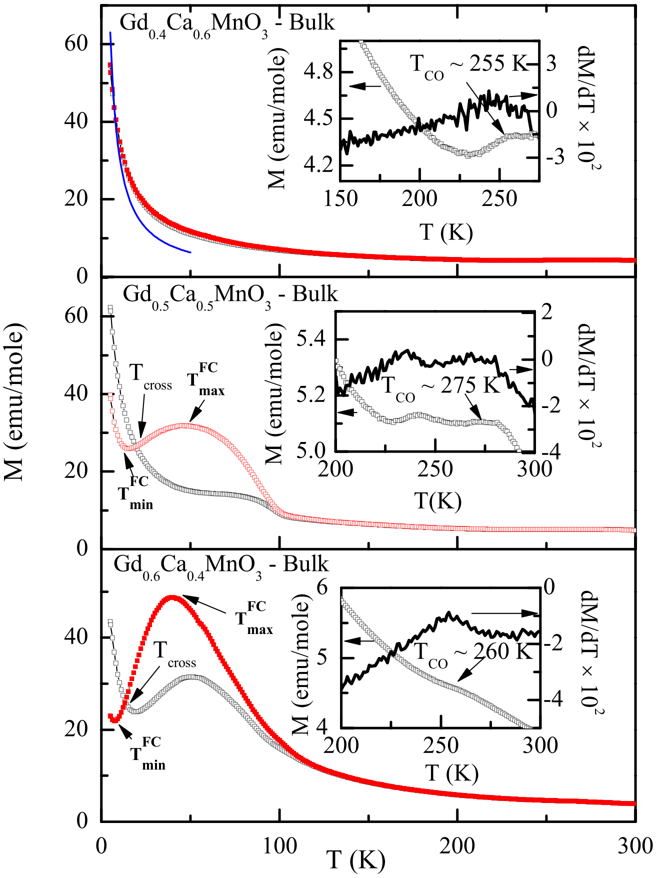

FIG. 3. Temperature-dependent magnetization of Gd$_{1-x}$Ca$_x$MnO$_3$-bulk ($x = 0.4$, 0.5, 0.6) at H = 100 Oe. FC (ZFC) data is plotted in red (black). Insets show the enlarged view of the magnetization curve (left axis) to point out the CO temperature and the corresponding peak in the derivative of magnetization curve (right axis). For $x = 0.6$ case, theoretical response for free Gd^{3+} ions (plotted in blue below 50 K) shows their dominant contribution to the total magnetization at lower temperatures.

A. FC and ZFC cases for weak external field

1. *Bulk samples*

We will first analyze the temperature-dependent magnetization M(T) curves for Gd$_{1-x}$Ca$_x$MnO$_3$-bulk ($x = 0.4$, 0.5, and 0.6), obtained under ZFC and FC conditions at 100 Oe external field, shown in Fig. 3. Enlarged view of the M(T) curves below 300 K, shown in the insets of Fig. 3, displayed discernible humps in the temperature range 255 K–275 K. The anomaly can, however, be prominently manifested on taking the derivative of the M(T) curves (see insets and their right axes in Fig. 3). This is a commonly observed behavior in many manganite systems including Gd$_{1-x}$Ca$_x$MnO$_3$ ($x \geqslant 0.5$) and has been explained to have arisen due to CO at temperature T$_{\rm CO}$ [39]. It may be noted here that the signature of CO in our samples has been extended even beyond the reported region of $x \geqslant 0.5$ (see Ref. [28]), as the same signature is observed in our Gd$_{0.6}$Ca$_{0.4}$MnO$_3$ sample [see Fig. 3 bottom (inset)]. Below T$_{\rm CO}$, in the temperature range 110 K–200 K, inverse susceptibility [χ^{-1}(T)] curves of all these compounds (as shown in Fig. 4) follow Curie-Weiss (CW)

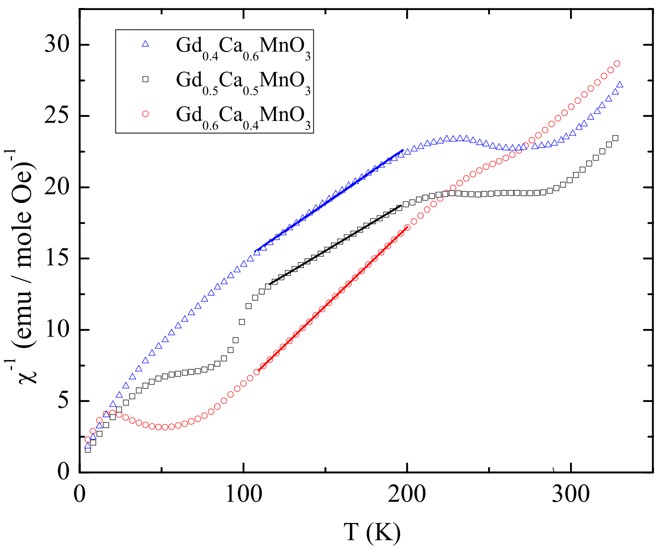

FIG. 4. Inverse magnetic susceptibility of bulk Gd$_{1-x}$Ca$_x$MnO$_3$ ($x = 0.4$, 0.5, 0.6) measured at 100 Oe under ZFC conditions. The linear regions, indicating Curie-Weiss behavior, are depicted by solid lines. In the depicted linear regions, ZFC and FC curves coincide as shown in Fig. 3.

behavior, i.e., a linear behavior with $\chi^{-1}(T) = (T - \theta_{\mathrm{CW}})/C$. For Gd$_{0.6}Ca_{0.4}MnO_3$, the values of θ_{CW} and C, as estimated from the CW behavior, are 44.7 K and 9.02 emu K/mole, respectively. The positive value of θ_{CW} indicates that the dominant exchange interaction is of the ferromagnetic type.

However, indicating antiferromagnetism, θ_{CW} is negative for Gd$_{0.5}$Ca$_{0.5}$MnO$_3$ and Gd$_{0.4}$Ca$_{0.6}$MnO$_3$ (as can be seen in Fig. 4); $\theta_{\mathrm{CW}} = -73.6$ K and $C = 14.49$ emu K/mole for Gd$_{0.5}$Ca$_{0.5}$MnO$_3$ and $\theta_{\mathrm{CW}} = -103.5$ K and $C =$ 9.00 emu K/mole for Gd$_{0.4}$Ca$_{0.6}$MnO$_3$. We note that the magnetic behaviors in our samples of $x = 0.4$, 0.5, and 0.6 are in agreement with those reported in Ref. [28].

Now, the system at $x = 0.4$, based on the phase diagram in Ref. [28] and Fig. 4, is primarily ferromagnetic with small domains that are AFM. Existence of small AFM domains at $x = 0.4$ is expected due to the doping proximity to $x = 0.5$ where the system is AFM; this will be further justified/clarified below. Hence, for the FC case, at temperatures T > T$_{\mathrm{Mn-Gd}}$, pertaining to the thermal energy larger than the magnetic energy for the weak AFM coupling $J_{\mathrm{Mn-Gd}}$, only the ferromagnetic fields (generated by the magnetic polarons) are relevant; here, ferromagnetism decreases with increasing temperatures. At temperatures below T$_{\mathrm{Mn-Gd}}$, the AFM coupling $J_{\mathrm{Mn-Gd}}$ starts becoming relevant and the Gd spins (with $S = 7/2$) in the percolating ferromagnetic cluster align antiparallel to the percolating cluster. At temperatures T < T$_{\mathrm{Mn-Gd}}$, the Gd spins that are aligned opposite to the percolating ferromagnetic cluster start lowering the overall magnetism. Contrastingly, the Gd spins in the small AFM domains start aligning (as temperature is lowered, i.e., for $T \lesssim 250$ K) due to the external weak magnetic field (H = 100 Oe) and contribute to increasing magnetism. This is because, *in the small AFM domains, there is no net coupling between* Gd *spins and the AFM lattice of* Mn *spins.* Needless to say that, when the Mn spins at the eight vertices of a unit cell are aligned antiferromagnetically, the total spin of the Mn spins at the eight vertices is zero; hence, when a Gd spin (with $S = 7/2$) is introduced at the center of the cube, the central Gd spin has no net coupling to the total spin of the eight vertices.

Now, the ZFC curve gives a picture that is qualitatively similar to that of the FC curve. However, the ZFC curve is further away from equilibrium compared to the FC curve because its ferromagnetic domains (compared to the FC case) are less aligned with the external field. This is because the starting state for the warming cycle of the ZFC case was obtained by cooling at zero field. Thus, the magnetization peak of the ZFC curve is lower than that of the FC curve. Consequently, there is a pronounced ZFC-FC bifurcation.

Next, at $x = 0.5$, based on the phase diagram in Ref. [28], the system is primarily AFM with small clusters that are ferromagnetic. In the FC case, the ferromagnetic clusters are strongly aligned with the external field and contribute to the magnetism similar to the larger ferromagnetic regions of the $x = 0.4$ case. Again, for the ZFC case, since the small ferromagnetic clusters are less aligned with the external field (than in the FC case), we get a smaller magnetization. Since the ferromagnetic domains are less dominant for the case of $x = 0.5$ compared to that of $x = 0.4$, the ZFC-FC bifurcation is less pronounced and the humps are also smaller for $x = 0.5$. Below T $\lesssim$ 250 K, the Gd spins in the large AFM domain start aligning due to the external weak magnetic field (H = 100 Oe) and contribute to larger magnetism compared to $x = 0.4$ case.

We also notice that the ZFC and the FC curves cross between the two magnetization extrema (i.e., the maximum and the minimum) for $x = 0.4$ and 0.5. The ZFC-FC crossover is obtained at T$_{\mathrm{cross}}$, below which the FC M(T) curve attains values lower than the ZFC M(T) curve. This is because the ZFC curves have larger AFM domains and smaller ferromagnetic domains (that are less aligned with the direction of H_{ext}) than the FC case. Furthermore, in the ferromagnetic domains at $x = 0.4$, the negative magnetization due to the Gd spins is more than the positive magnetization due to the Mn spins. In fact, based on the formula Gd$_{1-x}$Ca$_x$MnO$_3$, when Gd spins are antiparallel to the Mn spins and the weak external magnetic field, we can work out the effective spin of a unit cell to be $-\frac{7(1-x)}{2} + 2(1-x) + \frac{3x}{2} = -1.5 + 3x$; here, the axis of quantization is in the direction of the weak external field. Thus, at very low temperatures, magnetization in a cluster (containing ferromagnetic Mn sublattice) can be negative only when $-1.5 + 3x$ is negative, i.e., $x < 0.5$. In bulk samples at $x = 0.4$, as depicted in Fig. 3, it is important to note that the magnetism due to Gd spins in AFM clusters wins over the negative magnetization contribution from the ferromagnetic domains and keeps the magnetism positive, i.e., aligned with the external magnetic field.

Lastly, at $x = 0.6$, the system is essentially fully AFM. Thus, for both ZFC and FC cases, at lower temperatures only the Gd spins get more aligned due to the external weak magnetic field and magnetization increases in a similar fashion. Furthermore, as shown in Fig. 3, neither a ZFC-FC bifurcation nor a hump is visible due to negligible amount of ferromagnetic domains. Also plotted (in blue) is the paramagnetic response for free Gd spins $M = CH/T$ where $C = Ng^2S(S+1)\mu_B^2/(3k_B)$ with $S = 7/2$ and N being the number of Gd ions per mole; it is clearly demonstrated that paramagnetic

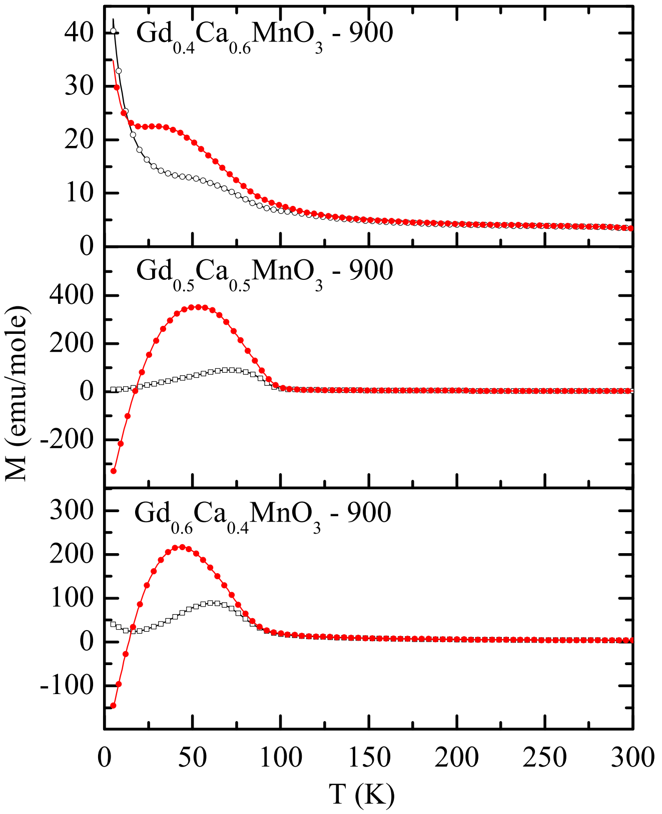

FIG. 5. Temperature-dependent magnetization curves of $Gd_{1-x}Ca_xMnO_3$-900 ($x = 0.4$, 0.5, 0.6) nanoparticles under a field of 100 Oe. FC (ZFC) data is depicted in red (black). The continuous lines are meant to be guides to the eye.

Gd ions in the AFM region give the dominant contribution at lower temperatures. As doping x increases, Gd concentration decreases resulting in smaller contribution to magnetization by the paramagnetic Gd spins at lower temperatures (compare magnetization values for $x = 0.6$ with those for $x = 0.5$ at $T < T^{FC}_{min}$ in Fig. 3).

It is also important to note that, since the CO energy scale [set by βE_p in Eq. (3)] is higher than both the ferromagnetic spin-order energy scale [set by $[t_{j,j+\delta} \cos(\theta_{j,j+\delta}/2)]^2/(2\gamma E_p)$ in Eq. (3)] as well as the AFM energy scale $J_{i,j}$ [mentioned in Eq. (4)], the charge ordering occurs at a much higher temperature than the magnetic ordering (as shown in Fig. 3).

2. Nanoform samples

Next, we will analyze the magnetization curves for manganites in nanoparticle forms at the same dopings $x = 0.4$, 0.5, and 0.6 as was done for the manganites in bulk form. To understand the observed magnetization in nanoparticles, we propose a plausible scenario of enhanced (reduced) Gd ion concentration at the surface (center) of the nanoparticles.

We did not observe any CO for the nanoforms of GCMO reported in this paper; this is in contrast to the bulk case where we witnessed CO (see Fig. 3). It is interesting to note that, for the lower-doped cases among the nanoforms considered, i.e., for $x = 0.4$ and 0.5 as shown in Fig. 5, we get negative magnetization at lower temperatures (i.e., $T \lesssim 20\,K$) for the FC case. In the nanoparticles, the unit cells are less rigid at the surface of the nanoparticles compared to the center. Consequently, it is natural that unit cells with smaller tolerance factors (which lead to distortion effects such as more buckling of Mn − O − Mn bonds) can be accommodated better at the surface than at the center. Hence, since the Gd ion has a smaller radius than the Ca ion, the concentration at the surface (center) of the nanoparticle for the Gd ions is higher (lower) than the overall stoichiometric concentration given by the formula $Gd_{1-x}Ca_xMnO_3$. Specifically, at $x = 0.4$ (0.5), the outer shell has less than 0.4 (0.5) holes per unit cell. It is important to realize that only when the effective concentration of Gd ions is more than 0.5 in a region can we get negative magnetization in that region; this is because then the average effective spin of Gd ions is $>7/4$ and the average effective spins of Mn ions $<7/4$ and the spins of Gd ions align antiparallel to those of Mn ions which are in the direction of the weak external magnetic field (H = 100 Oe). Furthermore, there is greater charge delocalization at the surface because CO is weaker here. Consequently, the charge polarizes beyond the NN, unlike the bulk situation modeled by Eq. (3); the

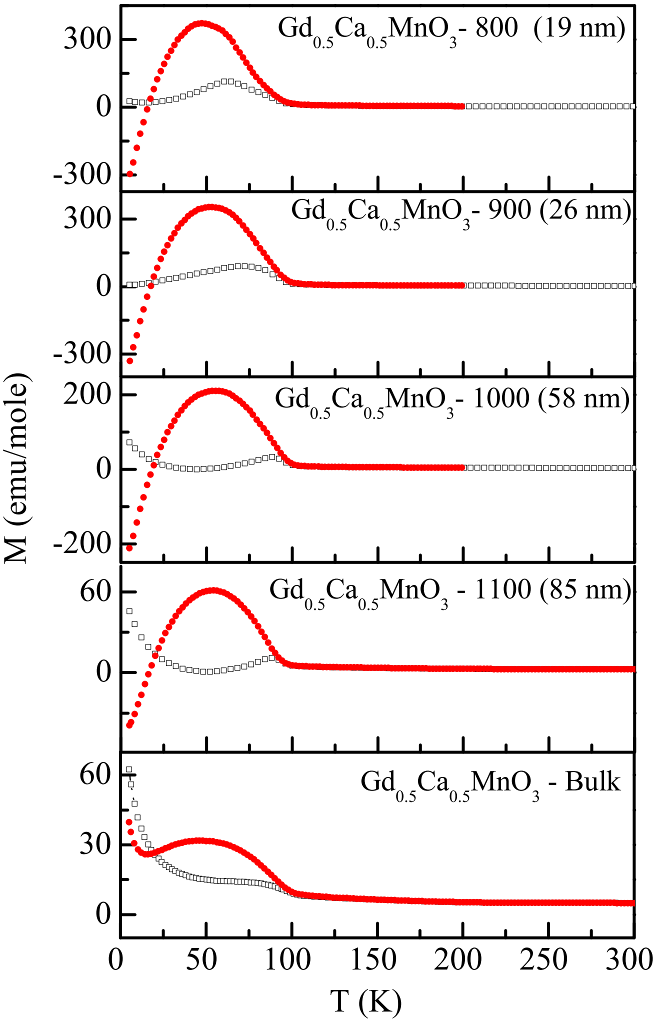

FIG. 6. Temperature-dependent magnetization curves of $Gd_{0.5}Ca_{0.5}MnO_3$, under a field of 100 Oe, for different annealing temperatures leading to different nanoparticle forms. The FC (ZFC) data is presented in red (black).

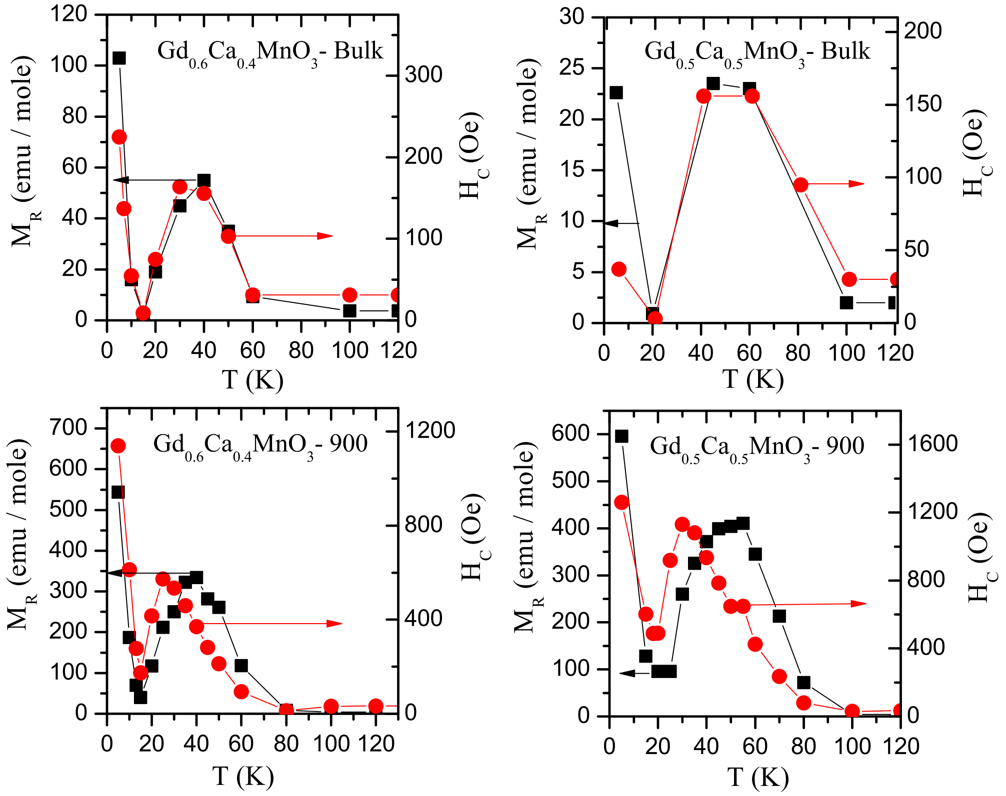

FIG. 7. Temperature dependence of remnant magnetization M_R and coercive field H_C obtained from magnetic hysterisis loops.

manganite in nanoparticle form is more ferromagnetic than in bulk form at the same effective concentration because of stronger double exchange phenomenon. For these reasons, compared to the bulk form, we have larger magnetism in nanoparticle form at higher temperatures and also larger negative magnetization at low temperatures. Accordingly, we see that the FC curves show large negative magnetization at low temperatures with the uncoupled Gd spins in the AFM core making only a weak positive magnetization contribution at low temperatures. Thus, the observed magnetism is most likely primarily from the outer shell for the cases $x = 0.4$ and 0.5. Furthermore, for the above mentioned reasons, the FC curve for the $x = 0.6$ nanosystem is similar to that of the bulk $Gd_{0.5}Ca_{0.5}MnO_3$ system with the peak magnetization being much smaller than at $x = 0.4$ and 0.5.

With regard to the the ZFC curves at $x = 0.4$, 0.5, and 0.6, since all the ferromagnetic domains are not fully aligned with the external field, we observe a weaker effect due to the outer shell. Unlike the FC curves, the ZFC curves are non-negative due to the fact that ferromagnetism is weaker when cooled in the absence of the external field; at lower temperatures, the negative magnetization resulting from the ferromagnetic outer shell is weaker than the positive magnetization resulting from the uncoupled Gd spins in the AFM core.

We now note that as particle size increases in various nanoforms of GCMO, the FC (ZFC) curves gradually tend toward the FC (ZFC) curves of the bulk system as expected. In confirmation, as particle size increases in Fig. 6 for $Gd_{0.5}Ca_{0.5}MnO_3$, the size of the hump decreases and the negative magnetization at lower temperatures reduces.

We will now make the important observation that negative magnetization at dopings $x = 0.4$ and 0.5 in nanoform GCMO is a metastable state because net magnetization is opposite to the applied field. Also, we expect ZFC curves to be further away from equilibrium than the FC curves because exposing the samples to magnetic field (while cooling) in the FC case helps them tend towards equilibrium. It is of interest to note that by and large the magnetization curves for the FC case (shown in Figs. 3 and 5) and the remnant magnetization M_R curves (depicted in Fig. 7) are similar at higher temperatures (i.e., $T > 20$ K). Thus, it is reasonable to expect that the FC curves and the remnant magnetization curves (obtained under very different conditions) are representative of the equilibrium physics at these higher temperatures (i.e., $T > 20$ K).

B. Remnant magnetization analysis at low temperatures

At lower temperatures (i.e., $T \lesssim 20$ K), we will analyze the remnant magnetization curves for the nanoparticle forms and the bulk forms separately. The expectation at equilibrium is that the Gd spins in the ferromagnetic regions will align with the external field whereas the Mn spins in the same regions will be antiparallel due to their AFM coupling to the Gd spins. At 5 K, although the nanoparticle forms in Fig. 7 display positive magnetization, they show much larger magnetization than when Gd spins are parallel to the external field and the Mn spins are antiparallel, i.e., much larger magnetization than obtained by reversing the sign of the magnetization in the nanoform curves for $x = 0.4$ and 0.5 in Fig. 5 at 5 K. Now, it is to be noted that during the isothermal magnetization measurements, due to exposure to high magnetic fields, the

Gd spins in the ferromagnetic regions will be aligned with the external field. Consequently, we infer that the Mn spins are not aligned antiparallel to the external magnetic field. Hence, the remnant magnetization curves also do not correspond to equilibrium.

With respect to the bulk forms at $T \lesssim 20\,\mathrm{K}$, for $x = 0.5$, as explained earlier, the magnetization due to Gd and Mn spins cancel each other in the ferromagnetic regions at low temperatures; the only contribution to magnetization is from the effectively uncoupled Gd spins in the AFM region. Thus, the equilibrium value of magnetization for $x = 0.5$ is expected to be similar to the FC value in Fig. 3, which is slightly higher than the remnant magnetization in Fig. 7.

Next, the bulk form at $x = 0.4$, in a unit cell, has an effective spin for the Gd ions ($=\frac{7(1-x)}{2} = 2.1$), which is larger than the effective spin for the Mn ions ($=2(1-x) + \frac{3x}{2} = 1.8$). Furthermore, the magnetization due to Gd ions in the ferromagnetic (AFM) regions $\mathrm{M}^{\mathrm{F}}_{\mathrm{Gd}}$ ($\mathrm{M}^{\mathrm{AF}}_{\mathrm{Gd}}$) and the magnetization due to the Mn ions in the ferromagnetic regions $\mathrm{M}^{\mathrm{F}}_{\mathrm{Mn}}$ together contribute as $-\mathrm{M}^{\mathrm{F}}_{\mathrm{Gd}} + \mathrm{M}^{\mathrm{F}}_{\mathrm{Mn}} + \mathrm{M}^{\mathrm{AF}}_{\mathrm{Gd}}$ at 5 K to the total magnetization $\mathrm{M}_{\mathrm{tot}}$ in Fig. 3. Then, based on the FC curve for $x = 0.4$ in Fig. 3, we see that at 5 K, $\mathrm{M}_{\mathrm{tot}} \sim 20$ emu/mole, $\mathrm{M}^{\mathrm{F}}_{\mathrm{Mn}} \sim 50$ emu/mole (based on FC curve value at 50 K), $\mathrm{M}^{\mathrm{F}}_{\mathrm{Gd}} \sim 50 \times 2.1/1.8 \sim 60$ emu/mole; consequently, at 5 K, $\mathrm{M}^{\mathrm{AF}}_{\mathrm{Gd}} = \mathrm{M}_{\mathrm{tot}} - \mathrm{M}^{\mathrm{F}}_{\mathrm{Mn}} + \mathrm{M}^{\mathrm{F}}_{\mathrm{Gd}} \sim 30$ emu/mole. For the bulk-form case of $x = 0.4$ in Fig. 7, where the remnant magnetization value is ~100 emu/mole at 5 K, it appears that the Gd spins in the ferromagnetic and AFM regions, when aligned parallel to the external magnetic field, contribute as $\mathrm{M}^{\mathrm{F}}_{\mathrm{Gd}} + \mathrm{M}^{\mathrm{AF}}_{\mathrm{Gd}} \sim 90$ emu/mole. This implies that the contribution of the Mn spins is ~10 emu/mole which is certainly not an equilibrium situation. At equilibrium, the magnetization contribution of the Mn spins should be negative (i.e., ~ -50 emu/mole).

It should also be noted that, as expected, the variation of the coercive field as a function of the temperature in Fig. 7 follows a trend that is similar to that of the remnant magnetization. Various details of the hysterisis loops are given in Appendix A.

C. FC and ZFC cases for stronger external fields

Lastly, we study the effect of stronger magnetic fields (i.e., fields stronger than 100 Oe) on the temperature dependence of magnetization in both bulk and in nanoparticle forms. In Fig. 8, we note that, as expected, at higher magnetic fields both the FC and ZFC curves for bulk and nanoforms of GCMO samples increase in magnetization and the curves shift upwards. We also see that, as applied magnetic field becomes stronger, in the lower-doped among the nanocompounds considered (such as $\mathrm{Gd_{0.5}Ca_{0.5}MnO_3}$), the system tends to attain an equilibrium state (with the Gd spins in the ferromagnetic regions tending to align with the external field), thereby becoming more prone to positive magnetization at low temperatures. Additionally, as the magnetic field increases, the degree of ZFC-FC bifurcation decreases; at sufficiently high fields, the FC and ZFC curves merge. The effect of increasing magnetic fields on the magnetization for bulk forms of GCMO at different dopings is shown in Appendix B. Furthermore, as the particle size increases in the lower-doped ones among the

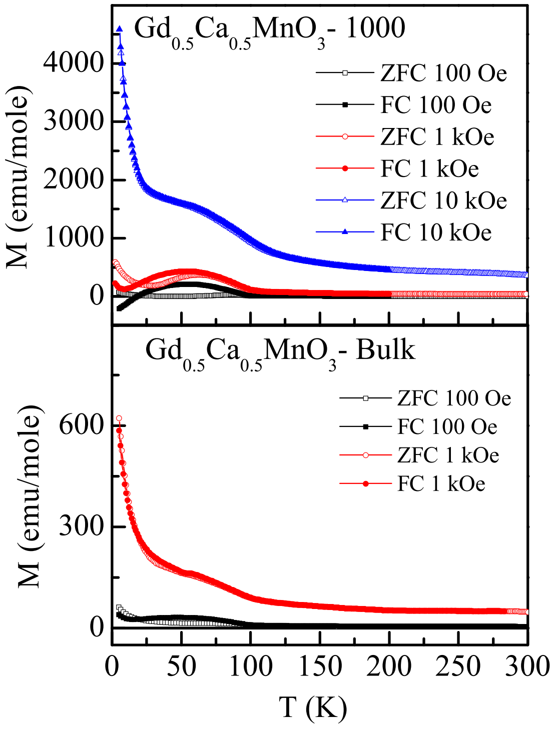

FIG. 8. Effect of different applied fields on the temperature-dependent magnetization curves of $\mathrm{Gd_{0.5}Ca_{0.5}MnO_3}$-bulk and $\mathrm{Gd_{0.5}Ca_{0.5}MnO_3}$-1000 systems.

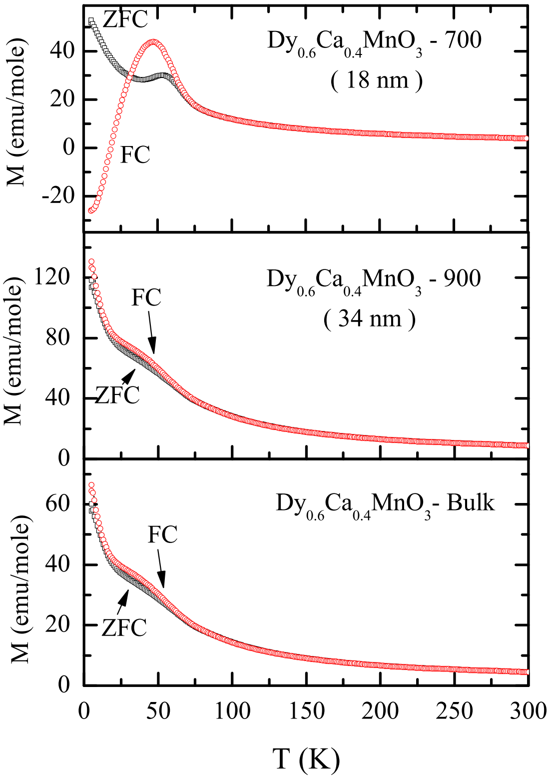

FIG. 9. Temperature-dependent magnetization curves of $\mathrm{Dy_{0.6}Ca_{0.4}MnO_3}$ for different particle sizes and annealing temperatures under a field of 100 Oe.

GCMO systems considered (such as $Gd_{0.5}Ca_{0.5}MnO_3$), there is a decrease in the magnetic field needed to produce positive magnetization and make the systems attain equilibrium at low temperatures, i.e., at $T \sim 5$ K (see Figs. 8 and 12).

V. CONCLUSION AND FUTURE DIRECTION

In this paper, by extending the framework developed earlier for ferromagnetic insulators [37] to ferrimagnetic insulators, we propose a mechanism for negative magnetization. Our plausible picture of negative magnetization, invoking surface effects of nanoparticles, is meant to interpret observed magnetization not only for the doping levels considered in this work (i.e., $x \geqslant 0.4$) but also for dopings lower than those considered. We also put forward an explanation of the size effect of the particles on negative magnetization in GCMO of various forms (i.e., bulk, thin film, and nanoforms).

In the future, experiments to probe the local concentration of Gd ions are needed to further validate our picture that, near the surface of nanoparticles, the concentration of Gd ions is higher than that indicated by the chemical fomula $Gd_{1-x}Ca_xMnO_3$. Making thin films and using cross-sectional transmission electron microscopy to measure the surface Gd-ion concentration as a function of depth is likely to clarify the situation.

It is also important to test the universal nature of our above-mentioned picture of negative magnetization phenomenon when other high-magnetic-moment, rare-earth ions are used in place of Gd ions in perovskite manganites. To this end, $Dy_{0.6}Ca_{0.4}MnO_3$ has been studied. This compound has been selected because, in the bulk form, it shows a slight ZFC-FC M(T) crossing but no negative magnetization in the FC M(T) curve whereas negative magnetization is observed at lower concentrations (i.e., $x = 0.2$, 0.25, and 0.3) [19].

Bulk form and variously sized nanoparticles of $Dy_{0.6}Ca_{0.4}MnO_3$ have been prepared and magnetization studies have been carried out. $Dy_{0.6}Ca_{0.4}MnO_3$ - bulk and $Dy_{0.6}Ca_{0.4}MnO_3$-900 nanoparticle sample show small bifurcations with small hump indicating ferromagnetic ordering. On further decreasing the particle size, $Dy_{0.6}Ca_{0.4}MnO_3$-700 nanoparticle system showed ZFC-FC crossing and negative magnetization in the FC curve (see Fig. 9). Thus, the emergence of negative magnetization in the nanoform of $R_{1-x}D_xMnO_3$ perovskite manganites (with R^{3+} being a high-magnetic-moment rare-earth ion) by controlling the system size seems to be a general phenomenon in manganites which needs extensive investigation.

We would like to point out that, although $Sm_{1-x}Sr_xMnO_3$ (for $x \leqslant 0.05$) shows negative magnetiztion [40], it belongs to a different type of system where a disordered paramagnetic sublattice is coupled with an ordered canted-AFM sublattice

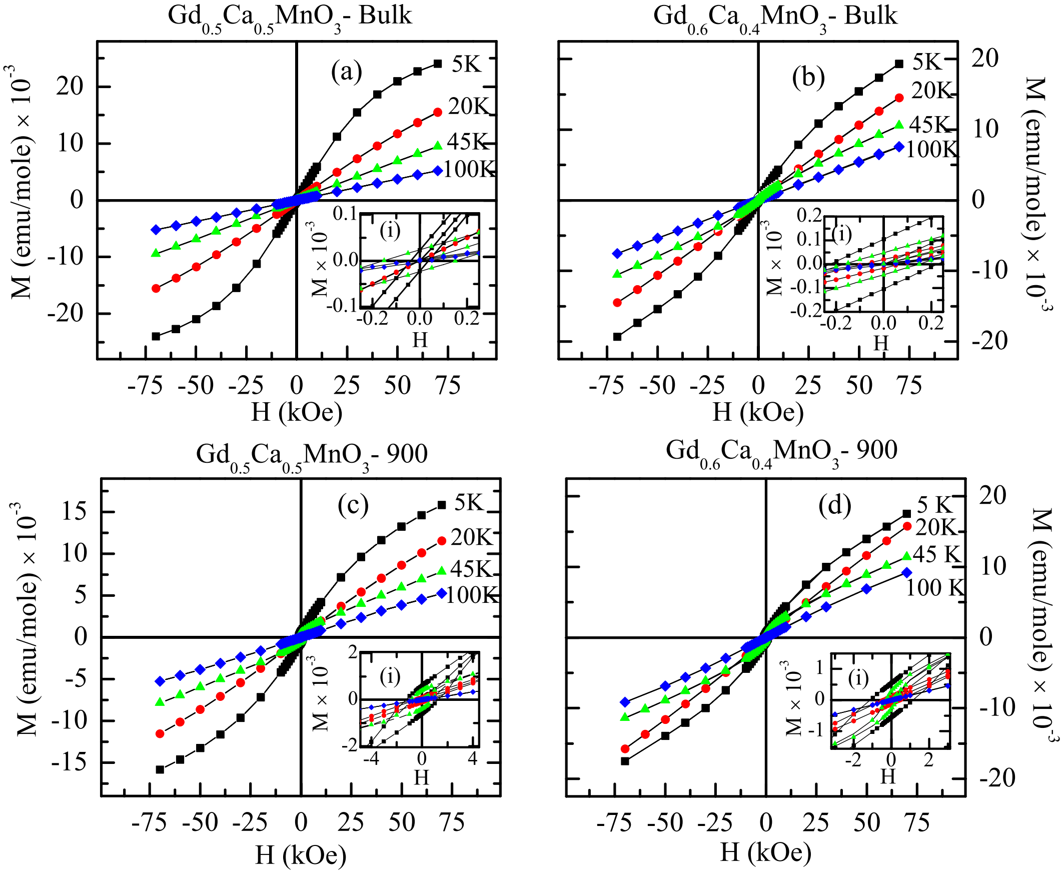

FIG. 10. Magnetization as a function of field at different temperatures in bulk and nanoform samples of $Gd_{1-x}Ca_xMnO_3$ at dopings $x = 0.4$ and 0.5. Inset shows enlarged version near the origin.

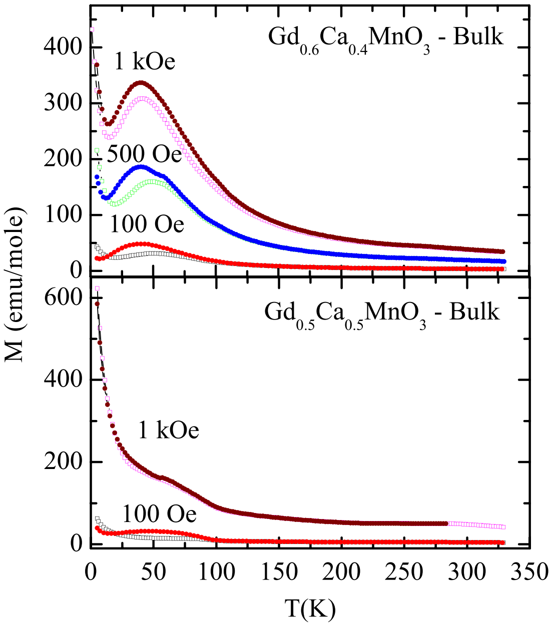

FIG. 11. Temperature-dependent magnetization curves under different applied magnetic fields in bulk $Gd_{1-x}Ca_xMnO_3$ (at $x = 0.4$ and 0.5). At any field, the FC curves have a higher peak.

via negative-exchange interaction. We aim to study such systems in future.

In the future, we also would like to examine the deeper connection between multiferroicity in RMnO$_3$ compounds (R= Gd, Tb, and Dy) [13–17] and negative magnetization that results when RMnO$_3$ systems are doped by divalent alkaline elements Sr, Ca, etc.

Lastly, it would be useful to develop materials with temperature-induced magnetization reversal in the vicinity of room temperature as they have potential for application in magnetic memories such as thermally assisted magnetic random access memory.

ACKNOWLEDGMENTS

S.Y. would like to acknowledge useful discussions with K. Pradhan, I. Das, and G. Baskaran. P.D. is thankful to the Department of Science and Technology (DST), India for financially supporting this study through the Women Scientist Project (Ref. No. SR/WOS-A/PM-24/2017).

APPENDIX A: HYSTERISIS LOOPS

The hysteresis curves, depicted in Fig. 10, reveal the expected features that as temperature decreases magnetization increases both in bulk and nanosamples; at lower temperatures, the curves tend toward saturation faster. The unusual and interesting trends of the remnant magnetizations (obtained from the hysteresis curves at various temperatures, dopings, and sample sizes) have been discussed in the main text.

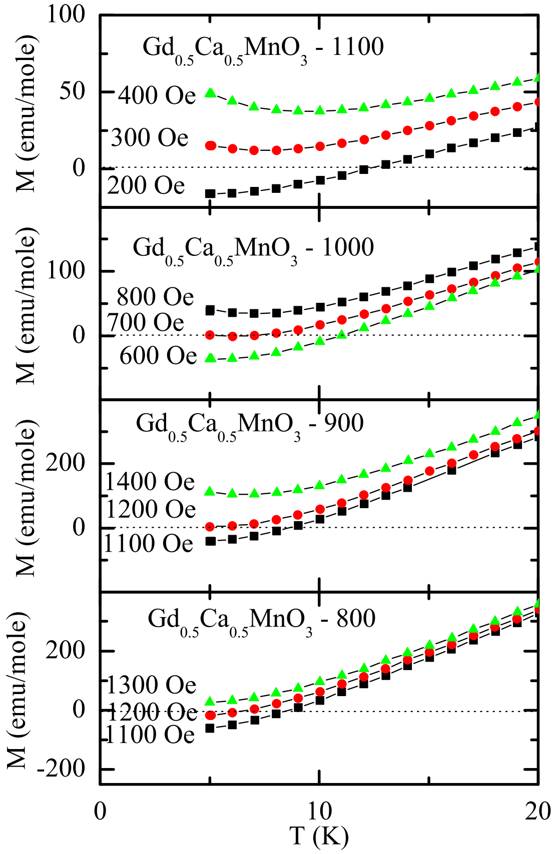

FIG. 12. Temperature variation of field-cooled magnetization curves M(T) under different applied magnetic fields in $Gd_{0.5}Ca_{0.5}MnO_3$-800, $Gd_{0.5}Ca_{0.5}MnO_3$-900, $Gd_{0.5}Ca_{0.5}MnO_3$-1000, and $Gd_{0.5}Ca_{0.5}MnO_3$-1100 nanoparticle samples.

APPENDIX B: BULK FORM MAGNETIZATION AT STRONGER MAGNETIC FIELDS AND VARIOUS DOPINGS

In Fig. 11, we depict that, as expected, the magnetization increases at higher magnetic fields for both the FC and the ZFC cases in bulk forms of GCMO samples; the curves shift upward. Furthermore, the ZFC-FC bifurcation reduces with increasing fields.

APPENDIX C: TRANSITION FROM NEGATIVE TO POSITIVE MAGNETIZATION DUE TO INCREASING MAGNETIC FIELD IN GCMO NANOPARTICLE SYSTEM

In Fig. 12, we demonstrate that, as the particle size increases in nanoform $Gd_{0.5}Ca_{0.5}MnO_3$, a smaller magnetic field is needed to produce a positive magnetization at lower temperatures.

---

[1] *Colossal Magnetoresistance, Charge Ordering, and Related Properties of Manganese Oxides*, edited by C. N. R. Rao and B. Raveau (World Scientific, Singapore, 1998).
[2] D. I. Khomskii, Phys. Scr. **72**, CC8 (2005).
[3] E. Dagotta, T. Hotta, and A. Moreo, Phys. Rep. **344**, 1 (2001).
[4] T. Hotta, Rep. Prog. Phys. **69**, 2061 (2006).

[5] Y. Tokura, Rep. Prog. Phys. **69**, 797 (2006).

[6] See K. H. Kim, M. Uehara, V. Kiryukhin and S.-W. Cheong, in *Colossal Magnetoresistive Manganites*, edited by T. Chatterji, (Kluwer Academic, Dordrecht, 2004).

[7] C. Martin, A. Maignan, M. Hervieu, and B. Raveau, Phys. Rev. B **60**, 12191 (1999).

[8] R. Pauthenet and C. Veyret, J. Phys. (Paris) **31**, 65 (1970).

[9] T. Kimura, S. Ishihara, H. Shintani, T. Arima, K. T. Takahashi, K. Ishizaka, and Y. Tokura, Phys. Rev. B **68**, 060403(R) (2003).

[10] R. D. Shannon, Acta Crystallogr. Sec. A **32**, 751 (1976).

[11] A. Kumar and S. M. Yusuf, Phys. Rep. **556**, 1 (2015).

[12] S. Biswas and S. Pal, Rev. Adv. Mater. Sci. **53**, 206 (2018).

[13] T. Kimura, T. Goto, H. Shintani, K. Ishizaka, T. Arima, and Y. Tokura, Nature (London) **426**, 55 (2003).

[14] T. Goto, T. Kimura, G. Lawes, A. P. Ramirez, and Y. Tokura, Phys. Rev. Lett. **92**, 257201 (2004).

[15] T. Kimura, G. Lawes, T. Goto, Y. Tokura, and A. P. Ramirez, Phys. Rev. B **71**, 224425 (2005).

[16] M. Kenzelmann, A. B. Harris, S. Jonas, C. Broholm, J. Schefer, S. B. Kim, C. L. Zhang, S.-W. Cheong, O. P. Vajk, and J. W. Lynn, Phys. Rev. Lett. **95**, 087206 (2005).

[17] T. Arima, T. Goto, Y. Yamasaki, S. Miyasaka, K. Ishii, M. Tsubota, T. Inami, Y. Murakami, and Y. Tokura, Phys. Rev. B **72**, 100102(R) (2005).

[18] O. Pena, M. Bahout, K. Ghanimi, P. Duran, D. Gutierrez, and C. Moure, J. Mater. Chem. **12**, 2480 (2002).

[19] M. M. Bahout, O. Pena, D. Gutierrez, P. Duran, and C. Moure, Solid State Commun. **122**, 561 (2002).

[20] G. J. Snyder, C. H. Booth, F. Bridges, R. Hiskes, S. DiCarolis, M. R. Beasley, and T. H. Geballe, Phys. Rev. B **55**, 6453 (1997).

[21] Y. Ma, M. Guilloux-Viry, P. Barahona, O. Pena, and C. Moure, Appl. Phys. Lett. **86**, 062506 (2005).

[22] Z. Yingnan, L. Junjia, Z. Ziqing, L. Fuyang, Z. Xudong, and L. Xiaoyang, Chem. Res. Chin. Univ. **31**, 699 (2015).

[23] B. S. Nagaraja, A. Rao, P. D. Babu, and G. S. Okram, Physica B **479**, 10 (2015).

[24] Y. Jin, X. P. Cui, J. A. Cheng, S. X. Cao, W. Ren, and J. C. Zhang, Appl. Phys. Lett. **107**, 072907 (2015).

[25] H. Nhalil and S. Elizabeth, J. Supercond. Nov. Magn. **30**, 1681 (2017).

[26] S. M. Yusuf, A. Kumar, and J. V. Yakhmi, Appl. Phys. Lett. **95**, 182506 (2009).

[27] A. Poddar, S. Das, and B. Chattopadhyay, J. Appl. Phys. **95**, 6261 (2004).

[28] A. Beiranvand, J. Tikkanen, H. Huhtinen, and P. Paturi, J. Alloys Compd. **720**, 126 (2017).

[29] C. Moure and O. Pena, J. Mag. Mag. Materials **337-338**, 1 (2013).

[30] A. Beiranvand, J. Tikkanen, H. Huhtinen, and P. Paturi, J. Mag. Mag. Mater. **469**, 253 (2019).

[31] J. Rodriguez-Carvajal, Physica B **192**, 55 (1993).

[32] P.-G. de Gennes, Phys. Rev. **118**, 141 (1960).

[33] Y. A. Izyumov and Y. N. Skryabin, Phys.-Usp. **44**, 109 (2001).

[34] H. Y. Hwang, S.-W. Cheong, P. G. Radaelli, M. Marezio, and B. Batlogg, Phys. Rev. Lett. **75**, 914 (1995).

[35] S. Paul, R. Pankaj, S. Yarlagadda, P. Majumdar, and P. B. Littlewood, Phys. Rev. B **96**, 195130 (2017).

[36] S. Datta, A. Das, and S. Yarlagadda, Phys. Rev. B **71**, 235118 (2005).

[37] S. Paul and S. Yarlagadda, Phys. Rev. B **103**, 035140 (2021).

[38] P. W. Anderson, Phys. Rev. **115**, 2 (1959).

[39] K. Das, T. Paramanik, and I. Das, J. Mag. Mag. Mater. **374**, 707 (2015).

[40] V. Yu. Ivanov, A. A. Mukhin, A. S. Prokhorov, and A. M. Balbashov, Phys. Stat. Sol. (b) **236**, 445 (2003).